AFRL-AFOSR-VA-TR-2023-0377

Metasurface Polarization Optics and Imaging

Capasso, Federico
HARVARD COLLEGE PRESIDENT & FELLOWS OF
1350 MASS AVE STE 600
CAMBRIDGE, MA,
US

06/27/2023
Final Technical Report

Air Force Research Laboratory
Air Force Office of Scientific Research
Arlington, Virginia 22203
Air Force Materiel Command

REPORT DOCUMENTATION PAGE

PLEASE DO NOT RETURN YOUR FORM TO THE ABOVE ORGANIZATION.

1. REPORT DATE	2. REPORT TYPE	3. DATES COVERED	
20230627	Final	START DATE 20210501	END DATE 20220430

4. TITLE AND SUBTITLE
Metasurface Polarization Optics and Imaging

5a. CONTRACT NUMBER	5b. GRANT NUMBER	5c. PROGRAM ELEMENT NUMBER
	FA9550-19-1-0135	61102F
5d. PROJECT NUMBER	**5e. TASK NUMBER**	**5f. WORK UNIT NUMBER**

6. AUTHOR(S)
Federico Capasso

7. PERFORMING ORGANIZATION NAME(S) AND ADDRESS(ES)
HARVARD COLLEGE PRESIDENT & FELLOWS OF
1350 MASS AVE STE 600
CAMBRIDGE, MA
US

8. PERFORMING ORGANIZATION REPORT NUMBER

9. SPONSORING/MONITORING AGENCY NAME(S) AND ADDRESS(ES)	10. SPONSOR/MONITOR'S ACRONYM(S)	11. SPONSOR/MONITOR'S REPORT NUMBER(S)
Air Force Office of Scientific Research 875 N. Randolph St. Room 3112 Arlington, VA 22203	AFRL/AFOSR RTB1	AFRL-AFOSR-VA-TR-2023-0377

12. DISTRIBUTION/AVAILABILITY STATEMENT
A Distribution Unlimited: PB Public Release

13. SUPPLEMENTARY NOTES

14. ABSTRACT
Using advanced design metasurface gratings were created; the significant step was taken of combining it with a conventional, intensity-only imaging system, converting it with just a single component into one capable of full-Stokes polarimetry. Using topology optimized metasurfaces were demonstrated with arbitrary shape birefringence. The latter has the unique feature that it can be continuously tuned from linear to elliptical birefringence by changing the angle of incidence. In this way, a single metasurface can operate as many waveplates in parallel, implementing different polarization transformations. Holograms were demonstrated that implement arbitrary parallel polarization analysis, as well as a hologram that implements
all birefringent waveplates simultaneously in its far-field. Metasurfaces were realized that
enact a longitudinally varying polarization behavior along the optical axis, implementing
virtual analyzers and waveplates with axes that rotate along the propagation direction. New
supercell metasurfaces were designed and implemented that exhibit multiple independent optical functions at arbitrary large deflection angles with high efficiency such as Gaussian, vortex and Bessel beams. 2D phase and polarization singularity sheets were realized. Singularity engineering of the “dark” enables new degrees of freedom for light-matter interaction and can inspire similar field topologies beyond optics, from electron beams to acoustics.
Accomplishments:
a. Imaging polarimetry with metagratings
b. Continuous angle-tunable birefringence with freeform metasurfaces
c. Jones Matrix Holography with metasurfaces
d. Metasurface optics for on-demand polarization transformations along the optical path
e. Multifunctional wide-angle optics based on supercell metasurfaces
f. Engineering 2D phase and polarization singularities

15. SUBJECT TERMS

16. SECURITY CLASSIFICATION OF:			17. LIMITATION OF ABSTRACT	18. NUMBER OF PAGES
a. REPORT	b. ABSTRACT	c. THIS PAGE		
U	U	U	UU	17

19a. NAME OF RESPONSIBLE PERSON	19b. PHONE NUMBER *(Include area code)*
GERNOT POMRENKE	426-8426

Standard Form 298 (Rev.5/2020)
Prescribed by ANSI Std. Z39.18

Final Performance Report
AFOSR Grant Number: FA9550-19-1-0135
Metasurface Polarization Optics and Imaging
Reporting Period: 05/01/2019-04/30/2022
Program Manager: Gernot Pomrenke

PI: Prof. Federico Capasso
John A. Paulson, School of Engineering and Applied Sciences
Harvard University
205A Pierce Hall,
29 Oxford St.
Cambridge MA 02138
Tel. 617-3847611
Fax 617-495-2875
Email: capasso@seas.harvard.edu

1. Goals

Polarization is a fundamental characteristic of electromagnetic radiation that describes the path the electric field sweeps in space. As such, its measurement is of great interest for remotesensing and imaging applications. Based on our initial work on metasurface-enabled polarimetry including single shot polarization sensitive cameras, which led to the demonstration of a single-shot polarization sensitive camera, this program focused on a broad research agenda consisting of investigating new frontiers in polarization optics including imaging, wavefront control, and structured light.

2. Accomplishments

a. Imaging polarimetry with metagratings

We previously demonstrated a new polarization-sensitive camera relying on gratings formed from an array of subwavelength-scale pillar elements possessing form birefringence These metasurface gratings are designed to direct most incident light into a finite set of diffraction orders with each order acting as an analyzer — a polarizer — for an arbitrarily specified polarization state. Measuring the intensity of four such orders yields enough information to determine the Stokes vector of light illuminating the grating over a photographic scene. Here we have taken the significant step of combining a suitably designed metagrating with a conventional, intensity-only imaging system, converting it with just a single component into one capable of full-Stokes polarimetry.

b. Continuous angle-tunable birefringence with freeform metasurfaces

Using topology optimized metasurfaces we have demonstrated arbitrary shape birefringence. Ithas the unique feature that it can be continuously tuned from linear to elliptical birefringence,by changing the angle of incidence. In this way, a single metasurface can operate as many waveplates in parallel, implementing different polarization transformations. Angle-tunable arbitrary birefringence expands the scope of metasurface polarization optics, enables compactand versatile polarization operations which would otherwise require cascading multiple elements, and may find far-reaching applications in polarization imaging, quantum optics andother areas.

c. Jones Matrix Holography with metasurfaces

We demonstrate holograms that implement arbitrary parallel polarization analysis, as well as a hologram that implements all birefringent waveplates simultaneously in its far-field. This customizable polarization transfer function devices may open new applications in a variety of fields of optics, including new approaches for point spread function engineering in precision optical systems (in e.g., reconnaissance systems and those intended for astrophysical measurements) and novel methods of polarization sensing.

d. Metasurface optics for on-demand polarization transformations along the optical path

We introduced metasurfaces that enact a longitudinally varying polarization behavior along the optical axis, implementing virtual analyzers and waveplates with axes that rotate along the propagation direction. The underlying principle is spatial polarization beating which allows an incident plane wave, after a single interaction with a metasurface, to encounter variable polarizer-like operations and/or waveplate-like transformations, locally, at each propagation plane in space thereafter.

e. Multifunctional wide-angle optics based on supercell metasurfaces

We have introduced a method based on supercell metasurfaces to demonstrate multiple independent optical functions at arbitrary large deflection angles with high efficiency. In one implementation the incident laser is simultaneously diffracted into Gaussian, helical and Bessel beams over a large angular range.. Our approach paves the way to novel methods to engineer the emission of optical sources.

f. Engineering 2D phase and polarization singularities

We show that two-dimensional (sheet) singularities can be engineered. We realize sheet singularities using metasurface by maximizing the field phase gradient at the desired positions. We experimentally realize phase and polarization singularity sheets with heart-shaped cross-sections using metasurfaces. Singularity engineering of the "dark" enables new degrees of freedom for light-matter interaction and can inspire similar field topologies beyond optics, from electron beams to acoustics.

3. Metasurface grating attachments convert existing camera systems into full-Stokes polarimeters with no active components

In our initial work we introduced "matrix Fourier optics" – a merger of concepts from the Jones calculus and Fourier optics. This matrix Fourier optics enabled us to design (and realize) diffraction gratings implementing arbitrary, parallel polarization analysis, a capability that had never been demonstrated in a single optical element. In that work, we combined a metasurface grating with a lensand a camera sensor to show how the grating could be used in a polarization imaging system. Since the primary focus of that work was on diffraction gratings, we sought to createas simple a camera as possible, just an initial proof-of-concept. An optical schematic of the camera prototype we constructed is shown in Fig. 1(b) (both in two- and three-dimensions). This enabled us to produce a simple imaging prototype, a packaged version of which isshown in Fig. 1(c).

However, the question of how best to integrate a diffraction grating with imaging optics to make a camera is far from trivial, and this initial approach was admittedly ad hoc. One of the goals of this program was to show that a suitable insertion of such a grating in front of a camera lens can realize a new camera prototype built around an existing imaging system.

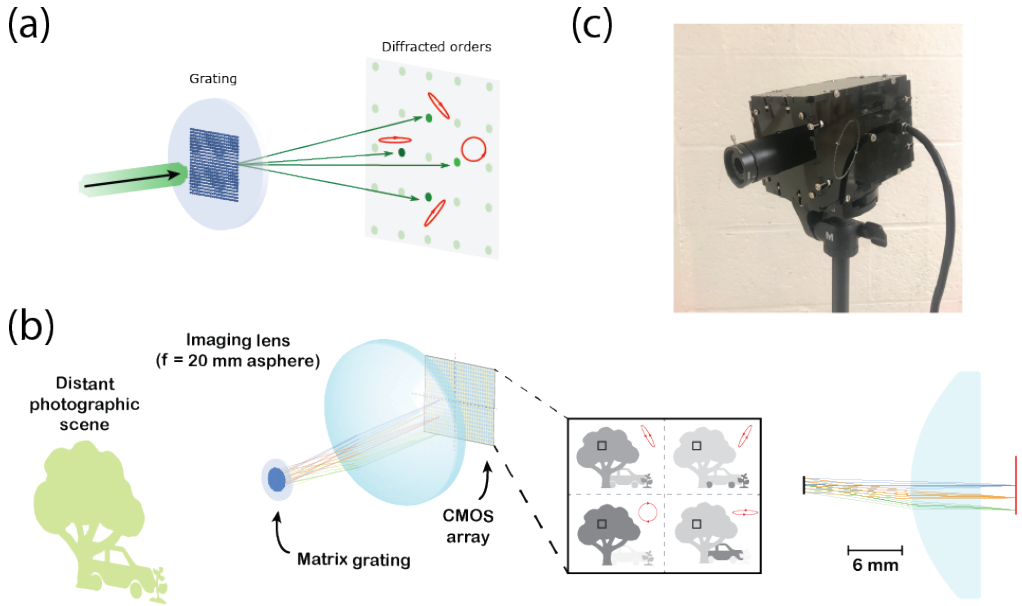

Fig. 1 Summary of previous work. (a) A metasurface polarization grating primarily directs light into a finite set of diffraction orders. The intensity of light in each order depends on the incident polarization state as though each order were a polarizer for an arbitrarily specified polarization state. **(b)** The orders from these gratings can be paired with an imaging system,in this case a rather arbitrarily selected aspheric lens, to form four images of a scene analyzed with respect to four different polarization states. These images can be combined to determine the Stokes vector over the scene. **(c)** Our previous packaged prototype based on this system.

Our chosen example system consists of a CMOS imaging sensor with a 1/1.8" format, roughly 7 mm × 5 mm in size (sensor: Sony IMX265, board and housing: IDS UI-3270LE) (Fig.2). Since we design around the assumption of a square sensor, we work the smaller dimension (5 mm) in what follows. The sensor is paired with a C-mount, fixed focal-length photographic objective lens with $f = 16$ mm. This pair represents a relatively generic imaging system for, e.g., machine vision applications. The unit cell of the grating used here is a 12 × 12 array of TiO2 pillars (each with a separation of 420 nm and a height of 600 nm) whose high index contrast with air in the visible (~2.3) and low loss enable shape-tunable, birefringent phase control. The parameters of each pillar (length, width, and orientation angle) in the grating's periodic unit cell are optimized to diffract as much light as possible into the innermost four diffraction orders of the grating while constraining these orders to act as polarizers for desired polarization states. The fabrication of these TiO2 metasurfaces was by electron beam lithography and atomic layer deposition. The parameters given above — a 12 × 12 array of pillars with 420 nm separation — give $D = 5.04$ µm and $\theta_{grating} = 6.0°$. The repeating unit cell of the grating is shown in Fig. 2(a), with a scanning electron micrograph (SEM) of the grating in Fig. 2(b). Next, we consider the polarimetric adaptation of the chosen lens with the designed metasurface grating and any tradeoffs involved. Figure 2(d) shows the adapted camera prototype.

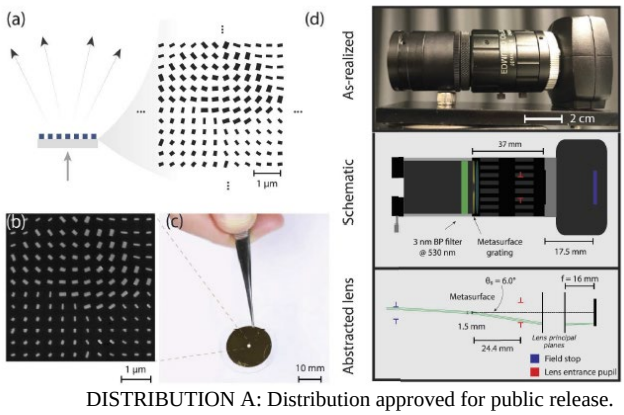

Fig. 2 Adaptation of an intensity-only imaging system with a metasurface polarization grating: (a) Schematic of the periodic unit cell of the metasurface design, composed of 12 × 12 TiO2 pillars 600 nm in height, each separated by 420 nm (yielding a diffraction angle compatible with the system being adapted). This unit cell is repeated ∼ 300 times in x and y to form a diffraction grating (chosen to be circular in profile) with a diameter of 1.5 mm. **(b)** A scanning electron micrograph (SEM) of the grating's unit cell. **(c)** The sample is fabricated on a 1" fused silica substrate and is surrounded by a metallic (gold) aperture to assure only light passing through the grating enters the imaging system. **(d)** The grating is mounted just in front of the front face of our chosen objective lens in a tube that also houses a bandpass filter centered at 530 nm and an adjustable iris functioning as a field stop. This is shown implemented (top), as a schematic (middle), and as a ray trace in which the lens is represented abstractly by its entrance pupil and principal planes. Simple trigonometry verifies that the extreme of the angular FOV can pass through the lens without vignetting.

Figure 3(b) shows four polarimetric image examples. We note here that applications of imaging polarimetry are wide-ranging, for applications as disparate as inspection of liquid crystal display panels during manufacturing, target detection, stress mapping, thin film thickness and refractive index measurement, solar magnetic field studies, and aerosol measurements. Consequently, the use of data from imaging polarimeters can vary from highly quantitative analysis (especially in remote sensing) to simple, qualitatively discerned visualization. The examples here (except for Fig. 3(ii)) show the polarized nature of specular, Fresnel reflection. Unpolarized light reflected from a specular surface becomes partially polarized in a direction perpendicular to the plane of incidence. Thus, polarization aids in identifying the azimuthal orientation of a specular surface's surface normal vector, that is, the surface normal 's projection in the viewing plane (with circular polarization information the zenith angle of the surface normal can also be determined). Figures 3(i) and (ii) were taken indoors under diffused LED illumination. In Fig. 3(i), the light polarized upon reflection from a soccer ball exhibits a major axis azimuth angle (often called Figures 3(i) and (ii) were taken indoors under diffused LED illumination. In Fig. 3(i), the light polarized upon reflection from a soccer ball exhibits a major axis azimuth angle (often called 'AoP' — angle of polarization) that sweeps between −90◦ and +90◦ from the perspective of the observer, passing through 0◦ on the top and bottom of the ball. The DoP shows that this light is only weakly polarized. Figure 3(ii) shows an assembly of Polaroid films with radially oriented transmission axes, easily seen in the azimuth image of the filters, while the DoP shows that light passing through the filters is highly polarized. Figures 3(iii) and (iv) are images taken outside under direct sunlight, including cars (often featured as demonstration targets in imaging polarimetry works). Smooth surfaces exhibit different orientations, such as the flat bench top in (iii) (0◦ azimuth) and the different car body panels in (iv). Variations in azimuth reveal changing surface features such as the curved back windshield in (iii). Here the DoP is strongest from the highly specular automobile glass surfaces.

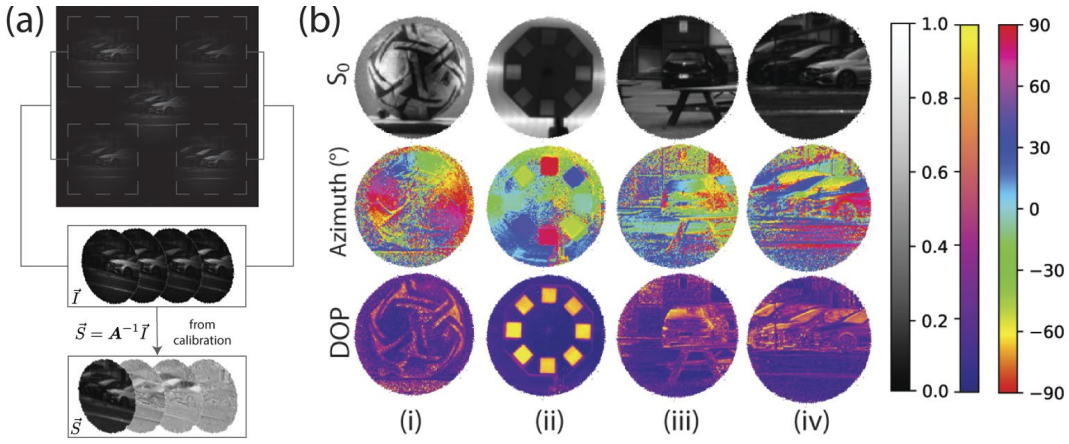

Fig. 3. Polarization imaging with adapted prototype: (a) A raw exposure is processed by selecting the four sub-images using a pre-characterized image registration. Using the pixel-wise instrument matrix from calibration, these can be converted into the four-element Stokes vector at each pixel. **(b)** Four imaging examples, two indoor (left) and two outdoor (right) are shown. These examples primarily explore the polarized nature of specular (Fresnel reflection), in which unpolarized light is partially polarized perpendicular to the plane of incidence upon reflection. In (i), a soccer ball illuminated with LED light shows an azimuth angle that varies around its edge, equal at diametrically opposite points, revealing its 3D shape. In (ii), light passing through a wheel of polarizing films is observed to be highly polarized relative to the background, with its polarization azimuth angle revealing the orientation of the filters. In (iii), a parked car and a picnic bench show smooth surfaces that polarize incident sunlight, revealing their orientation (such as the

top surface of the bench or the curved rear windshield of the car). DoP reveals that light from these specular surfaces is polarized relative to the background. Finally, in (iv), similar effects are observed in a row of parked cars where differently oriented panels of the car's bodies exhibit different azimuth signatures and high DoP

4. Continuous angle-tunable birefringence with freeform metasurfaces

Most existing birefringent devices, whether based on material- or shape birefringence are restricted to linear or circular polarization due to symmetry constraints. In general, to realize an arbitrary lossless polarization transformation requires having elliptical birefringence, i.e., birefringent components whose eigen-polarization states are elliptically polarized. Representing the most general case, it unlocks the full potential of polarization control: a single elliptically birefringent component can implement arbitrary unitary polarization transformation. However, so far, the capability to tailor arbitrary elliptical birefringence has not been explored. Also, since previous studies focus primarily on normal incidence operation, the angular dependence is usually ignored or treated as an unwanted artifact. The interplay between angle and polarization degrees of freedom in metasurfaces has remained largely unexplored. To address these limitations, we have utilized the adjoint-based topological optimization, a photonic inverse design technique, to engineer the birefringent response of metasurface elements. Topologicaloptimization allows the shape of nanostructures to be varied continuously in the design domain to minimize a given cost function subject to functional and geometrical constraints. Compared with the forward design strategy which relies on parameter sweeps of simple regular shapes, topological optimization provides a considerably larger design space, allowing searching for non- intuitive structures. This opens new possibilities to engineering unconventional birefringent response of metasurfaces.

Here, we intentionally tailor the desired elliptical birefringence as a functional feature. Using topological optimization, we demonstrate arbitrary shape birefringence (Fig. 4c) that addresses the above-mentioned limitations. It features a freeform shape, tailorable eigen- polarization states and designed angle tunability. It can be continuously tuned from linear birefringence to elliptical birefringence for various angles of incidence. At each fixed oblique angle of incidence, the tailored elliptical birefringence allows for versatile polarization transformation beyond what is achievable with previous single layer metasurfaces. For a range of angles of incidence, the designed angle tunability enables multifunctional polarization manipulation in momentum space. Our approach has a wide range of potential applications across industry and scientific research, such as momentum-space vector beam generation and polarization aberration correction in advanced optical systems.

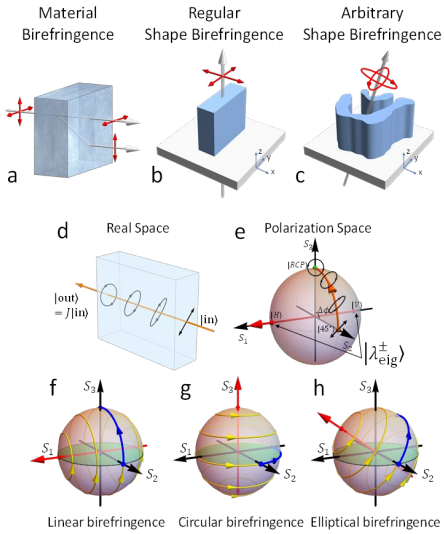

Fig. 4. **Concept of arbitrary elliptical birefringence**. (a) Material birefringence results from intrinsic material anisotropy. (b) Regular shape birefringence considers simple symmetric structures at normal incidence. The red arrows represent the linearly polarized eigenstates. (c) Arbitrary shape birefringence utilizes freeform structures to unlock novel polarization functionalities. In this work, we demonstrate a device that can be continuously tuned from linear birefringence to elliptical birefringence by varying the angle of incidence. The red arrows represent the elliptical eigen-polarization states at oblique incidence. (d) The evolution of polarization state of a light beam propagating through a quarter waveplate in the real space. (e) The same polarization evolution can be represented as a rotation (orange curve) in the polarization space (i.e., Poincaré sphere). (f-h) Polarization space representation of (f) linear, (g) circular and (h) elliptical birefringence. In general, birefringence induces a rotation of polarization states on the Poincaré sphere (along the yellow lines), with the rotation axis

(red axis) and rotation angle determined by the device's eigen-polarization states (red dots) and retardance respectively. The blue arrows show the trajectories for a quarter-wave retardance assuming a 45 deg linearly polarized incident light.

To provide an intuitive picture of this concept of arbitrary shape birefringence, we use the polarization space (Poincaré sphere) representation of birefringent components. Poincaré sphere is a graphical tool for visualizing polarization states. Each point on the surface of the sphere represents a fully polarized state, with the Cartesian coordinates given by the normalized Stokes parameters (S_1/S_0, S_2/S_0, S_3/S_0). The north and south poles represent right and left circular polarization and points on the equator correspond to linear polarization states. Using this picture, the polarization effects of birefringence can be elegantly described as a rotation on the Poincaré sphere, with the rotation axis and rotation angle determined by the eigen-polarization states $|\lambda_{eig} \pm \rangle$ and retardance $\Delta\phi$, respectively (Fig. 4E). As an illustrative example, the polarization effects of a conventional quarter–wave plate are shown both in real space (Fig. 1D) and on the Poincaré sphere (Fig. 4E). In real space, 45° linearly polarized incident light is gradually converted to right circular polarization at the output, $|45\circ\rangle \rightarrow |RCP\rangle$ (Fig. 4D). If we trace the polarization evolution on the Poincaré sphere, it follows a circular trajectory (Fig. 4E) that corresponds to a rotation around the S_1 axis by $\pi/2$. Note that the rotation axis connects the two eigen-polarization states, $|H\rangle$ and $|V\rangle$ in this case. The $\pi/2$ rotation angle results from the quarter–wave retardance ($\lambda/4$). This geometrical representation provides a unified picture for visualizing the polarization effects of different types of birefringence. Linear birefringence is represented by rotations on the Poincaré sphere around an axis that is limited to be within the equatorial plane (Fig. 4F). Circular birefringence features a rotation axis that coincides with the S_3 axis (Fig. 4G). Despite their prevalence, linear and circular birefringence constitutes only a small subset of all possible birefringence. Elliptical birefringence, in contrast, can take arbitrary rotation axes (Fig. 4H). It represents the most general type of birefringence and allows versatile polarization transformation beyond what is achievable with single linearly or circularly birefringent components.

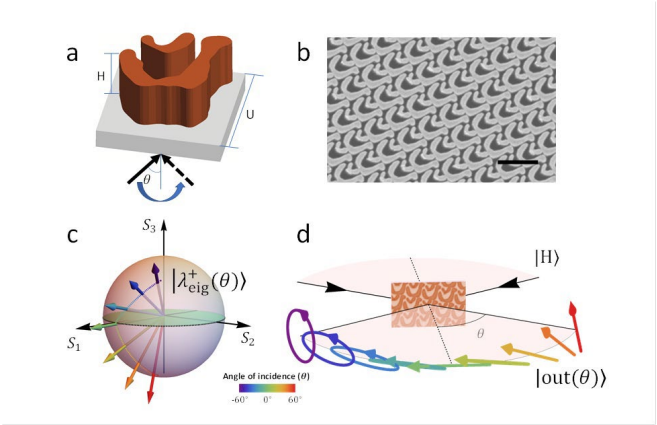

Fig. 5 Topology-optimized structure element. (a) Schematic of the optimized structure. It consists of freeform amorphous silicon (a-Si) nanostructures patterned on top of a glass substrate. The a-Si thickness is H=1500 nm. The center-to-center distance between neighboring elements is U=600 nm. (b) SEM image of a fabricated sample. Scale bar: 1 μm. (c) The arrows represent the angle-dependent eigen-polarization states of the device. Different colors correspond to different angles of incidence (θ). As one varies the angle, the device can be continuously tuned between linear and elliptical birefringence. (d) Angle-dependent polarization generation. For a fixed incident polarization (|in⟩=|H⟩), the output polarization state (|out(θ)⟩=J(θ)|H⟩) changes continuously from right circular polarization through horizontal linear polarization to 45^∘ linear polarization for varying angle of incidence.

The topology-optimized structure is shown in Fig. 5. It consists of 1.5 μm thick silicon nanostructures with optimized cross-sectional shape, on top of a glass substrate. The center-to-center distance between adjacent structures (U) is 600 nm. The design wavelength is 1550 nm. Fig. 5b shows a top-view SEM image of a fabricated sample. The functionality of our device can be illustrated on the Poincaré sphere (Fig. 5c). As the angle of incidence varies, the eigen-polarization state $|\lambda^+>$ follows a trajectory on the sphere that protrudes from the equator, showing the transition from linear to elliptical birefringence. For a fixed input horizontal linear polarization $|H\rangle$, the output polarization $|out\rangle=J|in\rangle$ is designed to change continuously from right circular through horizontal linear polarization to 45^0 linear polarization for various angles of incidence (Fig. 5d).

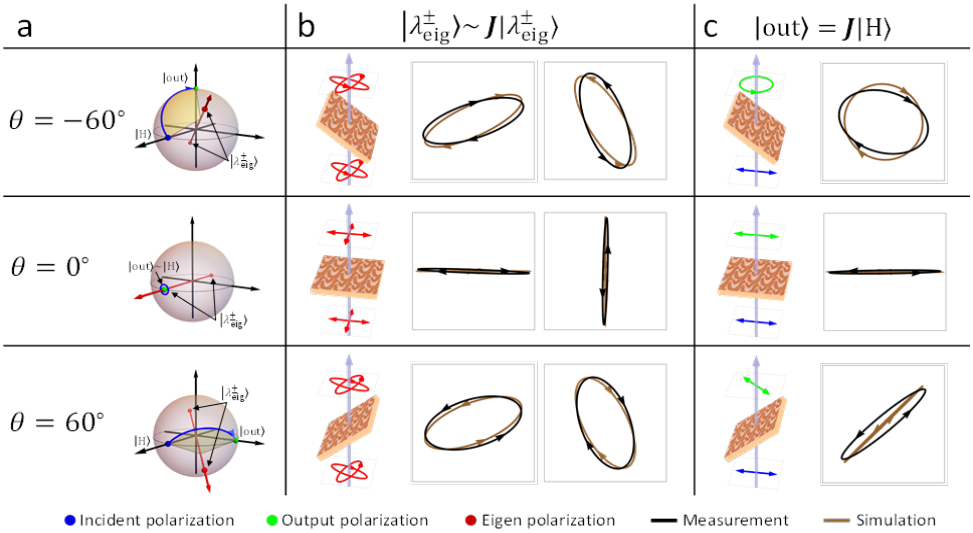

Fig. 6. Measurement results at the angles of incidence −60 , 0, and 60 deg. (**A**) Polarization space representation of the device functionality. At each angle, the device induces a rotation (blue arrows) on the Poincare sphere, which converts the input polarization ($|H\rangle$, blue dots) to the output polarization states ($|\text{out}\rangle$, green dots). The rotation axis (red arrows) is determined by the device's eigen-polarization states (red dots). (**B**) Measured (black) and simulated (brown) eigen-polarization states. One can see that at 60 the device is elliptically birefringent [corresponding to the out-of-equatorial-plane rotation axis in (A)], whereas at normal incidence, the device is linearly birefringent. At each angle, the two eigen-polarization states, are approximately orthogonal to each other. Note that the eigen-polarization states at 60∘ have opposite handedness. (**C**) Measured (black) and simulated (brown) output polarization states ($|\text{out}\rangle$) for a fixed incident polarization $|H\rangle$. By design, the output polarization becomes right circular polarization, horizontal linear polarization, and 45° linear polarization at −60∘, 0∘, and 60∘ respectively.

To fully characterize the device polarization response, Mueller matrix polarimetry was performed at various angles of incidence. Figure 6 shows the measured and simulated polarization states at $\theta = -60°, 0°, 60°$. The device's functionality is illustrated using the polarization space (Poincaré sphere) representation for each angle (Fig. 6a). Figure 6b shows the measured (black) and simulated (brown) eigen-polarization state, $|\lambda^{\pm}_{\text{eig}}\rangle \sim J|\lambda^{\pm}_{\text{eig}}\rangle$. We use the "∼" symbol instead of the equals sign because in general the eigenstate will acquire a phase shift. One can see that at normal incidence, $|\lambda^{\pm}_{\text{eig}}\rangle$ are linearly polarized, whereas at oblique incidence, $|\lambda^{\pm}_{\text{eig}}\rangle$ become elliptically polarized. Both the ellipticity and the orientation of the eigen-polarization ellipses differ significantly from that at normal incidence, proving the effectiveness of our design strategy. As expected from the unitarity of the Jones matrices, $|\lambda^{+}_{\text{eig}}\rangle$ and $|\lambda^{-}_{\text{eig}}\rangle$ are approximately orthogonal to each other at each angle of incidence. Note that the eigen-polarization states at $\pm 60°$ have opposite handedness. Figure 6c shows the output polarization states for a fixed incident state (horizontal linear polarization $|H\rangle$) . By design, the incident light is converted into right circular polarization $|RCP\rangle$, horizontal linear polarization $|H\rangle$ and 45° linear polarization $|45°\rangle$ at $\theta = -60°, 0°, 60°$ respectively (brown polarization ellipses). The measured output polarization states, $|\text{out}\rangle = J|\text{H}\rangle$, are shown in black in Fig. 6c. The measured degree of circular polarization (DOCP)(*14*) is 0.94 at $-60°$. Measured degree of linear polarization (DOLP) is 0.99 and 0.96 at $\theta = 0°, 60°$ respectively. The discrepancy between the simulation and measurement could be explained by fabrication errors such as structure dilation and inaccurate thickness Despite the difference, the phenomenon of interest – elliptical birefringence and unconventional angular dependence – remains robust.

5. Jones Matrix Holography with metasurfaces

In holography, a propagator, commonly the Fourier transform $\mathcal{F}$, links the "near-field"—an electric field with a phase and/or amplitude distribution created by a hologram—with the "far-field", a desired phase and/or amplitude distribution some distance many wavelengths away. Often, a hologram is described by its spatially varying, complex-valued aperture transmission function $t(x, y)$, a single complex-valued scalar function given by an amplitude and a phase. This picture can be generalized to handle polarization by describing the hologram instead by a 2×2 Jones matrix transfer function $\boldsymbol{J}(x, y)$ (matrix-valued quantities are denoted by bold lettering here). $\boldsymbol{J}(x, y)$ describes the polarization response at each point (x, y). Here we develop a top-level design of the

metasurface, specified *without* regard for any one incident polarization state. We describe a metasurface as a spatially varying Jones matrix $\boldsymbol{J}(x,y)$ and a far-field $\boldsymbol{A}(k_x,k_y) = \mathcal{F}\{\boldsymbol{J}(x,y)\}$ where the Fourier transform now distributes over all four elements (four complex-valued functions) of the Jones matrix as

$$\boldsymbol{A}(k_x,k_y) = \begin{bmatrix} \mathcal{F}\{J_{11}(x,y)\} & \mathcal{F}\{J_{12}(x,y)\} \\ \mathcal{F}\{J_{21}(x,y)\} & \mathcal{F}\{J_{22}(x,y)\} \end{bmatrix}. \qquad (1)$$

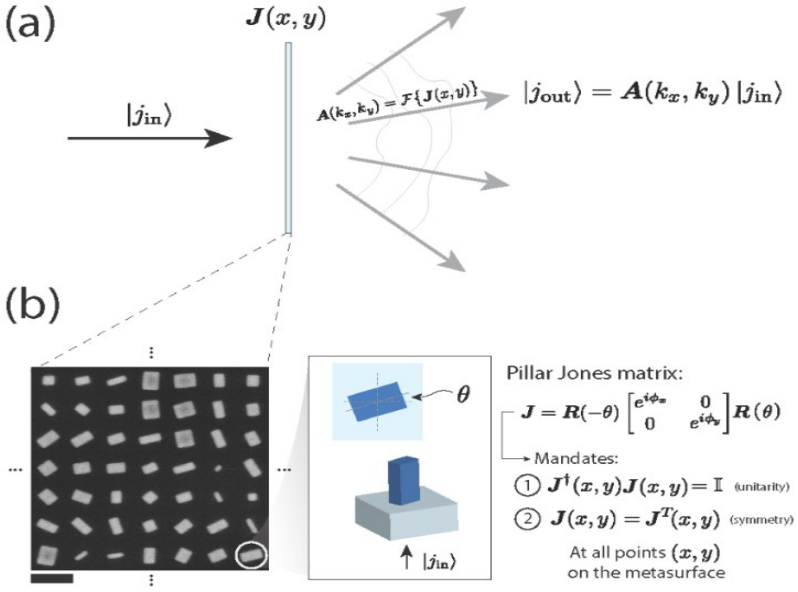

Fig.7 Jones matrix holography. (a) A Jones matrix hologram implements a polarization-dependent mask ($\boldsymbol{J}(x,y)$) with a far-field whose polarization response ($\boldsymbol{A}(k_x,k_y)$) whose behavior can be controlled. The far-field response to an incident polarization state with Jones vector $|j_{\text{in}}\rangle$ can be found by matrix multiplication. **(b)** These can be implemented with metasurfaces comprised of dielectric pillars, whose Jones matrices, as discussed in the text, are subject to certain mathematical constraints. An example SEM (scanning electron micrograph) of a small section of a sample from this work is shown (scale bar 500 nm).

If we assume plane wave incidence, $\boldsymbol{A}(k_x,k_y)$—itself a Jones matrix—gives the polarization-dependent behavior of each plane wave component (k_x,k_y) of the far-field (Fig. 7(a)). In other words, in this approach, rather than trying to control the far-field's intensity for some incident polarization or its polarization state we seek to control its polarization *transfer function*. For instance, if $\boldsymbol{A}(k_x,k_y)$ corresponds to an x polarizer, light will be directed into the plane wave component with direction (k_x,k_y) in a way that depends on the incident polarization state in accordance with a polarizer — bright if it is $|x\rangle$, dark if it is $|y\rangle$. Importantly, this matrix approach provides a method for realizing a desired, designer-specified custom polarization element.

If a far-field with a polarization-dependent response described by some $\boldsymbol{A}(k_x,k_y)$ is desired, a Jones matrix hologram implementing it is given by $\boldsymbol{J}(x,y) = \mathcal{F}^{-1}\{\boldsymbol{A}(k_x,k_y)\}$.

An optical element must realize the spatially varying Jones matrix $\boldsymbol{J}(x,y)$. A dielectric metasurface is a natural choice here. The pillars of a dielectric metasurface can implement the behavior of a waveplate whose retardance, overall phase, and angular orientation can vary arbitrarily as

$$\boldsymbol{J}(x,y) = \boldsymbol{R}(-\theta)\begin{bmatrix} e^{i\phi_x} & 0 \\ 0 & e^{i\phi_y} \end{bmatrix}\boldsymbol{R}(\theta) \qquad (2)$$

In other words, a metasurface can implement any symmetric, unitary Jones matrix. The Jones matrix hologram $\boldsymbol{J}(x,y)$ implied by a desired far-field behavior $\boldsymbol{A}(k_x,k_y)$ must obey these constraints to be realizable by a metasurface. To guarantee matrix symmetry, any desired $\boldsymbol{A}(k_x,k_y)$ must be symmetric at all points in the far-field (some consequences of this are discussed below). To guarantee unitarity, a matrix generalization of the well-known Gerchberg-Saxton phase-retrieval algorithm can be used.

Polarization-analyzing holograms

An ideal polarizer passes a preferred polarization state $|\lambda\rangle$ (elliptical in general) without attenuation while extinguishing the orthogonal state $|\lambda^{\perp}\rangle$ with $\langle\lambda|\lambda^{\perp}\rangle = 0$. Here we demonstrate Jones matrix holograms whose far-fields implement designerpolarizer-like behavior. That is, holograms whose far-fields implement the polarization transfer function $\boldsymbol{A}(k_x, k_y) = a(k_x, k_y)|\lambda^*(k_x, k_y)\rangle\langle\lambda(k_x, k_y)|$ where the amplitude a and polarization state being analyzed $|\lambda\rangle$ can each vary independently and arbitrarily across the far-field. Thus, the far-field of a Jones matrix hologram can be engineered to implement arbitrary, parallel polarization analysis. Fig. 8 makes this capability tangible with a simple example. A dielectric metasurface can be designed and fabricated based on a given design. In this case, the metasurface implements a Jones matrix mask $\boldsymbol{J}(x, y)$ whose far-field contains holographic images of different polarization ellipses (eight linear states of varying orientation and both circular polarization states). The region containing each image acts as a polarization analyzer for its respective, depicted polarization state. For example, the holographic image of $|x\rangle$ (horizontal arrow) is brightest when the incident polarization $|j_{\text{in}}\rangle = |x\rangle$ and dark when $|j_{\text{in}}\rangle = |y\rangle$, as though the pixels contained within the drawing act as an analyzer of $|x\rangle$ polarized light. The schematic of the far-field shown in Fig. 8(a) shows all polarization ellipses equally bright for clarity's sake; this would be the case only if the incident light were perfectly unpolarized, with equal projection onto all polarization states. As shown in Fig.8(a), the fabricated metasurface is illuminated with collimated laser light (λ = 532 nm in this case) of variable polarization. The angular spectrum (far-field) that resultsis imaged onto a CMOS sensor using a relay setup filtering out the non-diffracted zero order along the way.

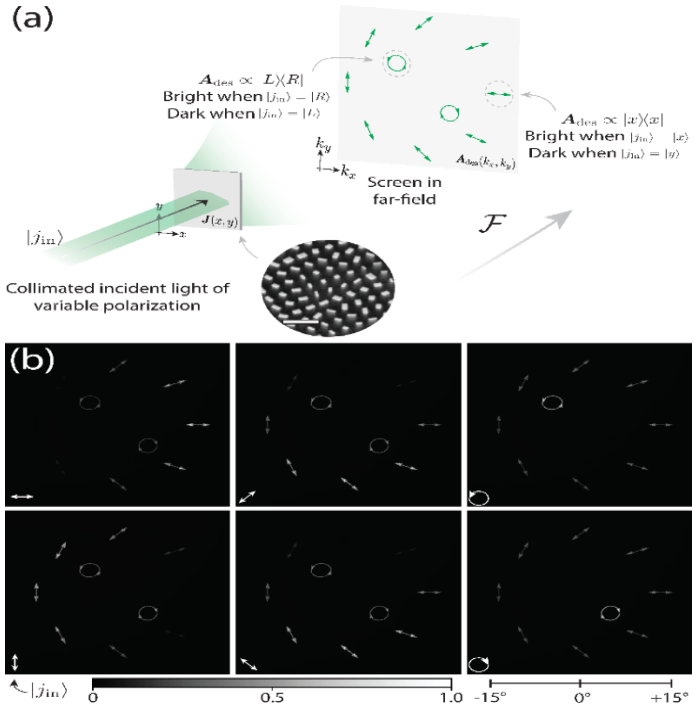

Fig. 8 Parallel polarization analysis by a Jones matrix hologram. (a) When illuminated with collimated laser light, a suitably designed metasurface hologram implements a far-field in which light is directed on the basis of its incident polarization state. In this particular example, the hologram is designed to produce a pattern of illustrations of different polarization states. Each drawing acts as an ``analyzer'' for its depicted polarization state. For instance, the drawing of x-polarized light (horizontal line) is bright when $|j_{\text{in}}\rangle = |x\rangle$ and dark when $|j_{\text{in}}\rangle = |y\rangle$ – this part of the far-field implements the Jones matrix $\boldsymbol{A}(k_x, k_y) = |x\rangle\langle x|$. (SEM scale bar is 1 micron). **(b)** The far-field measured on a CMOS sensor reflects this desired behavior for six incident polarization states (incident polarization $|j_{\text{in}}\rangle$ is denoted in white at the lower left of each image). The right scale bar shows the cone angle subtended by the far-field, while a color bar denotes the image intensity.

Fig. 8 (b) shows the far-field produced by the metasurface hologram for six incident polarization states, each of which is denoted in the bottom left corner of its image by a white label. As can be seen, each incident polarization state prompts the strongest response in the region of the hologram corresponding to itself. For example, $|j_{\text{in}}\rangle = |45°\rangle$ prompts the hologram to direct most power to the drawing of diagonal, linearly polarized light, while the image of anti-diagonal polarization is dark with a gradient in-between, while drawings of $|x\rangle$, $|y\rangle$, $|R\rangle$, and $|L\rangle$ are allabout half as bright. When each circular polarization is incident, all linear polarizations are about equally bright (and half as bright as the image of the incident circular state, all in accordance with Malus' Law. In a way, then, the hologram of Fig. 8 is a "visual full-Stokes polarimeter " from which an incident polarization state can be simply read out by inspection.

Similarly, holograms with a far-field exhibiting waveplate-like behavior can be created. This work may find application in a variety of areas. A Jones matrix hologram could add custom polarization-dependence to an optical system's point spread function, either to addresses systematic polarization aberrations in precision imaging systems or to enable wholly new functions. Elements based on spatially varying liquid crystals are already employed in astrophysical measurements for, e.g., exoplanet detection; the present work, and the expanded control it offers, may suggest new possibilities there. Active photonic platforms provide a second promising application area. Light distribution in the holograms of this work is governed by linearity and Malus' Law. Gain-associated nonlinearities in, e.g., a laser cavity could potentially surmount this, enabling applications such as polarization-dependent beam steering.

6. Metasurface optics for on-demand polarization transformations along the optical path

These devices can reduce a system of conventional polarization optics, arranged along the optical path, into a single meta-optic, allowing remote control of polarization in 3D. Although our polarization meta-optics are static, they produce different 3D structured light patterns at the output in response to changing the input polarization. In essence, the incident polarization acts as a knob for the device, enabling an adaptive response and leading to many technological consequences, for e.g., varifocal lenes and axicons, and can benefit light-matter interaction and laser micromachining in 3D.

Our approach relies on the Jones matrix formalism. The transverse components of the electric field are expressed as a 2D Jones vector whereas the polarizing element is expressed as a 2-by-2 Jones matrix. Hence, a longitudinally variable polarizing element—one that changes its polarization response as a function of distance—translates to a 2-by-2 Jones matrix that varies along the optical axis. To realize this, we revisited the idea of spatial harmonic beating as illustrated in Fig. 9(a): two plane waves with the same frequency and polarization, but slightly different axial propagation constants k_z, realized by changing their tilt angle relative to the z-axis, undergo intensity beating in their envelope. If we expand this scalar picture and allow the polarization of each wave to differ, the polarization state of the ensemble will be modulated with propagation. This is depicted in Fig. 9(b) where the same two waves, now circularly polarized with opposite handedness, yield a waveform that rotates its linear polarization as it propagates. This picture is the cornerstone of longitudinally variable polarization control based on digital holography which assume that the input polarization is predetermined; that is, other incident polarizations cannot be handled using the same setup. To tackle this, we allow our waveforms to be weighted by Jones matrices rather than Jones vectors.
Our devices implement a superposition of co-propagating Bessel functions, with equal separation in k_z-space, each weighted by a different 2-by-2 matrix, as shown in Fig. 9(c). The choice of the Bessel functions is not fundamental but rather advantageous since Bessel beams—traditionally generated from axicons—are favored for their diffraction-resistant, pencil-like, and self-healing nature, which serve our aim for constructing a longitudinally variable response over a long range.

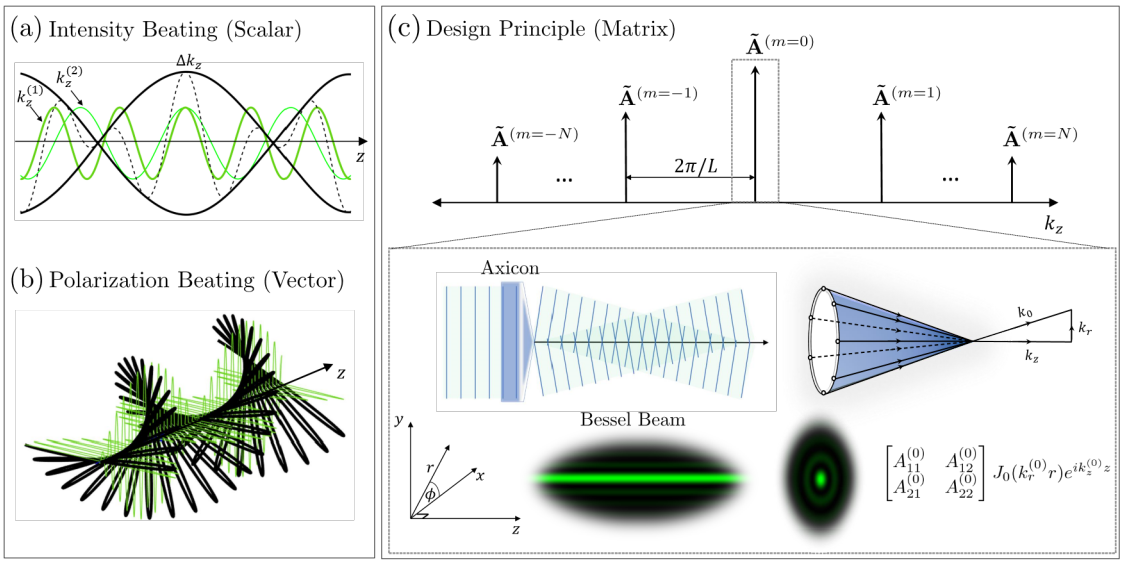

\

Fig. 9. Concept of longitudinally variable polarization elements. (a) Intensity beating between two monochromatic plane waves (green) with the same frequency but slightly different propagation constants, $k_z^{(1)}$and $k_z^{(2)}$, achieved by changing their tilt angle with respect to z-axis, produces amplitude modulation in the resulting waveform (dashed black curve) and its envelope (solid black curve). (b) Polarization beating produced by interfering two vector waves with the same frequency but different propagation constants, k_z, and different polarization. Here, the two interfering waveforms are circularly polarized with opposite handedness leading to a linearly polarized waveform (black) that rotates its polarization with propagation. The green curves are the orthogonal components of the black waveform projected on the vertical and horizontal planes. (c) Design principle: the polarizing device implements a superposition of 2N+1 Bessel functions with equal separation of $2\pi/L$ in k_z. The inset depicts a Bessel beam generated by an axicon and its decomposition into plane waves whose wave vectors lie on the surface of a cone. Each Bessel function in the sum has a slightly different cone angle and is weighted by a 2-by-2 Jones matrix, $\tilde{A}^{(m)}$.

To achieve this task, we deployed metasurfaces consisting of linearly birefringent nanofins which can, point-by-point, be regarded as tunable waveplates, imparting a phase shift between $[0,2\boldsymbol{\pi}]$ along its two anisotropic axes. Due to the lossless nature of these waveplate-like pixels, however, this metasurface scheme does not modify the amplitude of incident light, only its retardance. To overcome this obstacle, we developed a new matrix-based holographic technique which allows us to control not only the polarization and phase but also the amplitude across the output wavefront.

The devices were fabricated via e-beam lithography and atomic layer deposition. The devices have been characterized using a standard 4-$\boldsymbol{f}$ lens system used to filter and image the response of the metasurface onto a CCD camera. The output beam was then recorded using a CCD camera that samples along the $\boldsymbol{z}$-direction, where $\boldsymbol{z = 0}$ plane lies at the output focal plane of the second lens of the **4-$\boldsymbol{f}$** system. To characterize the polarization behavior of the output beam at each $\boldsymbol{z}$-plane, we performed polarization measurements based on Stokes polarimetry. This enabled the determination of the Stokes vector, which quantifies the polarization ellipse at each point.

We fabricated and tested a longitudinally variable linear analyzer whose transmission axis virtually "rotates" its orientation (ϕ) with respect to the x-axis as a function of z. The states of polarization being analyzed for vary continuously from $\hat{x}$ (0°) to $\hat{y}$ (90°) between $z = 2.5$ mm to $z = 5.5$ mm. Figure 10 (a) illustrates the analyzer's response. Under x-polarized incident illumination, the on-axis intensity decays gradually while propagating away from the device until it is nearly quenched at $z = 5.2$ mm. This is in accordance with the z-analyzer's *virtual* transmission axis, as depicted by the red arrows, and Malus' law. In contrast, under $\hat{y}$ illumination, the on-axis intensity increases over the same space region. Here, the extinction ratio between the two is on the order of -20 dB.

Note that since the polarizing metasurface is comprised of unitary (lossless) waveplate-like unit cells, the loss mechanism here relies on the judicious interference among the propagating modes. The beams generated from our device are characterized by a diffractionless Bessel-like transverse profile, as depicted in Fig. 10 (b).

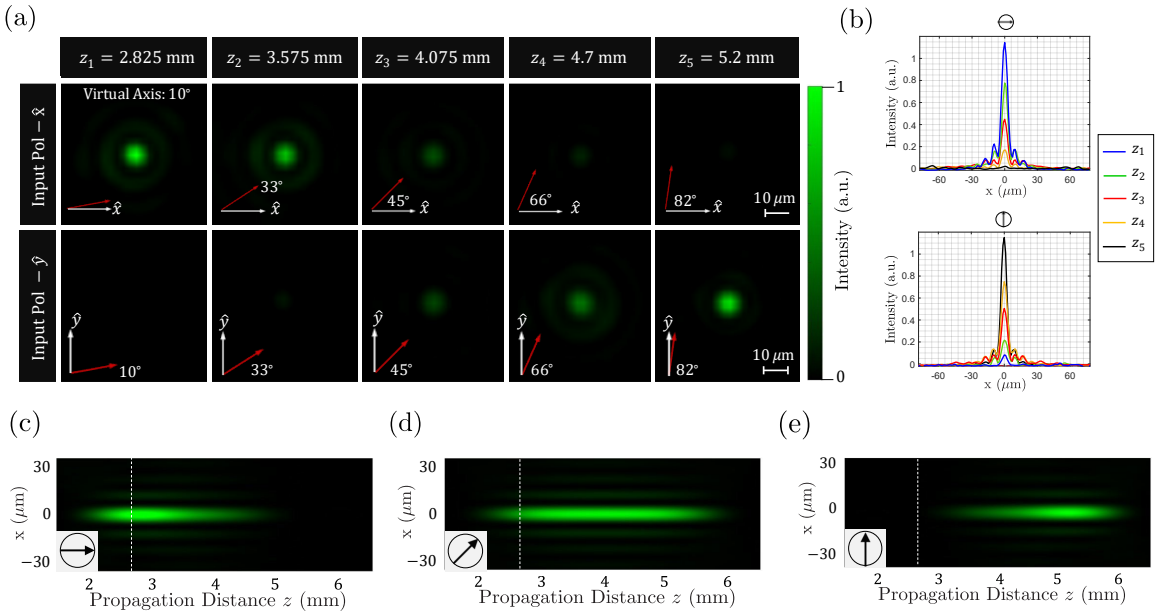

Fig. 10. **Longitudinally variable analyzer**. **(a)** Measured transverse profiles of the output beam at different planes along the propagation direction for $\hat{x}$ and $\hat{y}$ incident polarizations. The white arrows depict the incident polarization whereas the red arrows represent the state of polarization being analyzed for by our device at each z- plane. **(b)** Intensity cross-sections for the output

beam at the five *z*-planes in (a). **(c-e)** Longitudinal profile of the generated pencil-like beam for each incident polarization depicted in the inset. The centroid of the on-axis intensity distribution continuously shifts away from the dashed white reference line in response to rotating the input polarization from 0° to 90°.

Figures 10 (c-e) show the pencil-like longitudinal profile of the output beam where the centroid shifts back and forth along the optical path in accordance to rotating the incident polarization. In addition to tailoring diattenuation along the *z*-direction, our approach is more general and can be applied to engineer retardance, as discussed next.

The polarization-tunable axicon previously discussed may be exploited in optical trapping to push/pull a microparticle along the optical path by changing the input polarization. It can also be used to spatially tailor the excitation of optically pumped media. Further, if illuminated by a partially polarized beam, our devices can change the degree-of-polarization of output light with propagation. Structured light with varying polarization may also suggest new schemes in sensing since polarization rotation is a function of the optical length. These devices can also spatially modulate the spectrum of quantum emitters, control the shape and size of laser-machined structures, and to enhance optical chirality in light-matter interaction, therefore opening many new paths**.**

7. Multifunctional wide-angle optics

Metasurfaces suffer from limited performance and efficiency when multiple functions with large deflection angles are required because the *non-local* interactions due to optical coupling between nanostructures are not fully considered. Here we present a new method based on supercell metasurfaces to demonstrate multiple independent optical functions at arbitrary large deflection angles with high efficiency.

The simplest approach to multifunctional metasurfaces is based on the use of local subwavelength unit cells that are designed to impart a *local* phase or polarization profile to light propagating through the cell. In the simplest case, a library of unit cells can be prepared changing some physical parameters in the cell and simulating its transmission phase. By "*local"*, we refer to the fact that cells are designed separately and inter-cell coupling effects are neglected or limited to the assumption of a perfectly periodic array using Bloch or periodic boundary conditions. This causes a significant loss of efficiency and other undesired effects when large deflection angles are required. Specifically, the latter need large phase gradients which may be under-sampled by common unit cells. Multiple functions such as focusing, holograms, polarization functions and beam shaping can then be achieved by designing separated metasurfaces (one for each function) and interleaving the cells in a compound metasurface. This approach is however highly inefficient.

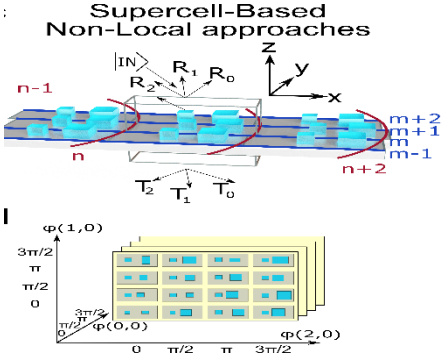

Fig. 11 The generalized supercell metasurface concept. Top**:** Unlike subwavelength unit cells, supercells possess multiple diffraction orders that depend on the coupling between the supercell elements. This non-locality becomes important as the deflection angle increases and can be rigorously taken into account in the design. Bottom: , An example of multidimensional library of non-local supercells. The library contains a supercell for each possible combination of phases for all the orders.

One can overcome locality using supercells instead of unit cells. Within this approach, adjacent cells are merged into a supercell containing multiple metaatoms. These can be directly designed and simulated by considering non-local effects due to the optical coupling between the metaatoms. In this work we have introduced supercell metasurfaces (SCMS) based on a library of supercells to enable the realization of multiple functions with large deflection angles without a loss of efficiency (Fig 11). Using supercells as the building block of our library, we exploit the fact that the coupling between neighboring metaatoms in the supercell can re-distribute optical power within the supercell. This

enables a transmission/reflection amplitude that can locally exceed unity, breaking the locality constraint of multifunctional local metasurface approaches and enabling multifunctionality with high efficiencies at large deflection angles.

Each supercell in the library is optimized to achieve specific transmission phase and amplitude in each order. Different phase profiles can be implemented on each order by selecting at each position of the metasurface the supercell that satisfies simultaneously the phase requirement for all orders. The required phase profile of a certain order can be calculated by the inverse Fourier transform of the far field of this respective function only. This allows us to demonstrate independent functions at different and large angles.

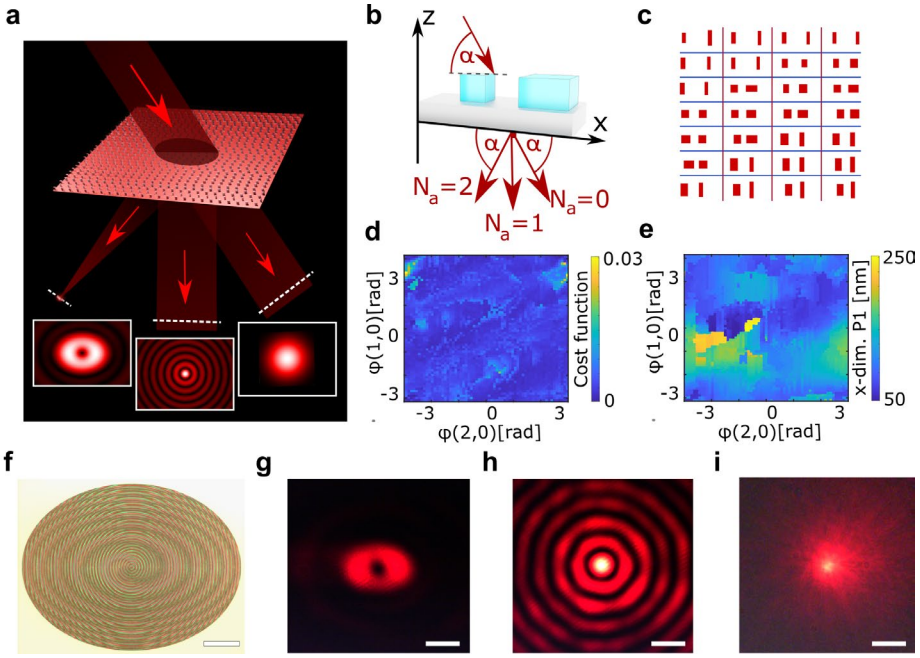

Fig. 12 | Multifunctional beam shaping supercell metasurface (SCMS). **a**, Schematic and simulation results. The collimated input beam has a gaussian profile and impinges under a steep angle (52°). The SCMS splits the beam into a gaussian, a Bessel- and a focused helical beam while introducing a deflection of 0°, 52° and 104°, respectively. **b**, Schematic of the two-pillar supercell. **c**, Schematic of a metasurface detail. All supercells have the dimension of 800nm×400nm. **d**, Optimization results of the supercell library showing the cost function for a 2π phase coverage on the orders (1,0) and (2,0). **e**, Optimization results of the supercell library showing the x-dimension of the first pillar for a 2π phase coverage on the orders (1,0) and (2,0). **f**, Optical image of the fabricated SCMS. Scale bar 165 μm. **g**, Optical measurement of the focused helical beam. Scale bar: 8 μm. **h**, Optical measurement of the Bessel beam. Scale bar: 8 μm. **i**, Optical measurement of the 0th order in the far field.

As a first example, we present a SCMS that splits a collimated, s-polarized light beam, that is incident under a large angle of 52°, into three independent beams with large difference in angle (Fig. 12a). Specifically, the zeroth order remains a gaussian beam, the first order is bend by 52° and shaped into a Bessel beam and the second is focused under an angle of 104° while imparting orbital angular momentum (OAM), creating a singularity in the focus. The simulated far fields of the orders are shown in the framed insets in the same schematic. While the large deflection of the beams is controlled by the supercell periodicity, the functions are implemented by changing the supercell inlay at each lattice position. By choosing all supercells to have the dimension of 800nm × 400nm, the supercells are subwavelength in *y*, but have two additional orders in *x* (Fig. 12). By placing the supercells on a regular grid, the metasurface will then deflect the two additional orders by the desired angles of 52° and 104°, respectively. The functions are implemented by an additional superposed phase profile, which is slowly varying and can be sampled from a library with the same phase in order (0,0) for all library elements and a 2π phase coverage in both additional orders (1,0) and (2,0). Figure 12 d, e are graphical representations of the cost function *f* and an example of a supercell parameter of each supercell library element with *f* defined as:

$$f = \sum_{j=0}^{2} \left| A_j \cdot e^{i\phi_j} - A_{j,\text{target}} \cdot e^{i\phi_{j,\text{target}}} \right|^2 \qquad (3)$$

with A_j and ϕ_j being the simulated amplitude and phase of order j, and $A_{j,\text{target}}$ and $\phi_{j,\text{target}}$ are the corresponding desired amplitude and phase of order j. The optical image (Fig. 12f) shows the superposition of the characteristic spiral and the concentric rings required for a focused OAM and a Bessel beam, respectively. The measured beams agree with the designed profiles (Fig. 12g-i)

8. Engineering 2D phase and polarization singularities

Optical phase singularities are positions of zero field value in a complex scalar field – regions of darkness surrounded by light. These singularities are ubiquitous in complex wave systems and are typically accompanied by extremely rapid phase variation nearby. Optical singularities are widely synonymous with one-dimensional (1D) singularity lines, such as those on the optical axis of orbital angular momentum or vortex beams. This interchangeability often creates a misconception that all optical singularities look like 1D lines, where the propagation phase swirls around the central linear singularity, thereby undermining 0D and 2D singularities.

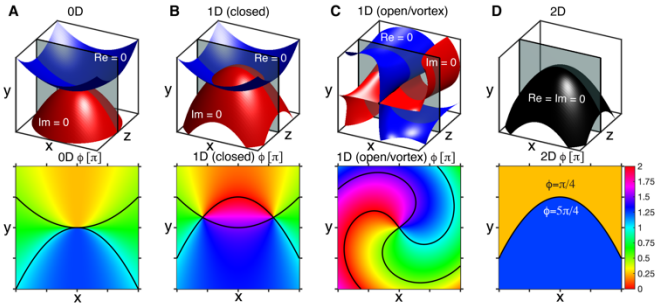

Fig. 13 Phase singularities are formed at the intersection of the zero-isosurfaces of the real (Re) and imaginary (Im) parts of a complex field. Top row: Intersection topologies of the two zero-isosurfaces (blue: Re=0, red: Im=0). Bottom row: Phase profiles for each intersection topology in the top row, evaluated at the grey cross-sectional plane. Black lines indicate the zero-valued contours on the plane. (**A**) When the zero-isosurfaces intersect at a point, a 0D point singularity is formed. 1D singularities can be formed as (**B**) a closed loop or (**C**) an open line. The fundamental vortex beam, with its corkscrew-like zero-surfaces, is plotted in (**C**). (**D**) When the zero-isosurfaces are equal, the singularity is 2D.

The most commonly referenced optical singularity, phase singularities, occur where real and imaginary parts of a scalar electromagnetic field $E(\boldsymbol{r})=\text{Re}[E(\boldsymbol{r})]+i\text{Im}[E(\boldsymbol{r})]$ are simultaneously zero, leaving the propagation phase undefined there. The points at which the real (or imaginary) part of the field vanishes typically forms a surface. The field zeros and optical singularities both occur at the intersection of these two zero-surfaces. The intersection may occur at exactly one point, forming a 0D singularity (Fig. 13A). However, when the intersection between the two zero-surfaces forms a line, a 1D linear singularity is produced. The intersection locus can be a closed loop (Fig. 13B) or open line (Fig. 13C). In one instance of the latter, the widely known vortex beam in Fig. 13C, the real and imaginary parts form corkscrew-like isosurfaces that only intersect on the optical axis. Notably, when the zero-valued real and zero-valued imaginary surfaces coincide, a 2D "sheet" singularity is produced (Fig. 13D). A simple example of such a singularity is the radial nodes in Bessel beams. However, there has been a lack of further investigation of such 2D sheet singularities due to them being less common and more unstable.

Singularities are closely associated with infinities in the spatial gradients of field parameters. Hence, singularity engineering singularities does not rely on optimizing the field parameters (such as phases), but rather on their spatial gradients. Phase singularities are intimately connected to phase gradients, which rise to arbitrarily large values in the vicinity of a singularity. This connection between singularities and parameter gradients motivates our approach to designing the dark. *We maximize the spatial derivatives of field parameters as a proxy for enforcing singular behavior.* As such, the field value can be made vanishingly small and the phase gradient can be made arbitrarily large, allowing these positions to behave as actual optical singularities for all practical purposes.

We exhibit this capability through two designs. The first is a 2D phase-singularity sheet with an engineered heart-shaped cross-section. This is generated by maximizing the phase gradient in the directions oriented normally to the target heart-shape at a target z=10 mm plane. Fig. 14B shows an isosurface plot of the simulated low field intensity region to depict the orientation of the designed 2D singularity in 3D space. The cross-sectional simulated intensity and the phase plots of the designed 2D singularity at the z=10 mm plane (grey plane in Fig. 14B) are shown in Fig. 13C-D. The optimization parameters are the propagation phase delay at each pixel on a wavefront-controlling surface located at z=0 mm. We fabricated a phase-only metasurface (Fig. 14A), comprising TiO_2 nanopillars on a fused silica substrate that enforces this required phase profile. The intensity and phase profiles produced at the z=10 mm plane are plotted in Fig. 14 E-F and are in good agreement with simulation. Further, the rapid intensity decay along the singularity sheet (~ -35 dB), stemming from our phase gradient optimization, can be observed in the plots.

We also demonstrate 2D polarization singularities (specifically, C singularities in a paraxial field) in analogy to phase singularities. Instead of the phase being singular, the polarization azimuth Ψ is singular at the singularity loci. Since 2Ψ is the complex argument of the Stokes field $\Sigma_{12}=s_1+is_2$, by maximizing the phase gradient of Σ_{12}, one is maximizing the polarization azimuth gradient, and thereby producing a polarization singularity. Fig. 14H exhibits the cross-section of an engineered polarization singularity with an azimuth jump that follows a heart-shaped trajectory. The heart-shape and position are identical to that of the previous phase. The polarization singularity requires a device that can control the point-by-point polarization of a wavefront. One such device is a polarization-sensitive metasurface [5], which we fabricated using anisotropic TiO_2 nanofins on fused silica (Fig. 14G). The experimental measurement of the polarization azimuth at z=10 mm is plotted in Fig. 14I and it exhibits close correspondence to the simulation prediction. Although not shown, these 2D singularities exhibit very rich angular momentum dynamics compared to their 1D counterpart.

To the best of our knowledge, these are the first demonstrations of custom singularity shaping beyond curved lines. Beyond optics, singularities are common in many complex wave systems, such as acoustic, fluidic, and plasmonic systems. We expect that similar strategies of optimizing spatial gradients and higher order derivatives will enable one to engineer complex fields imbued with the strange behavior of nearby singularities.

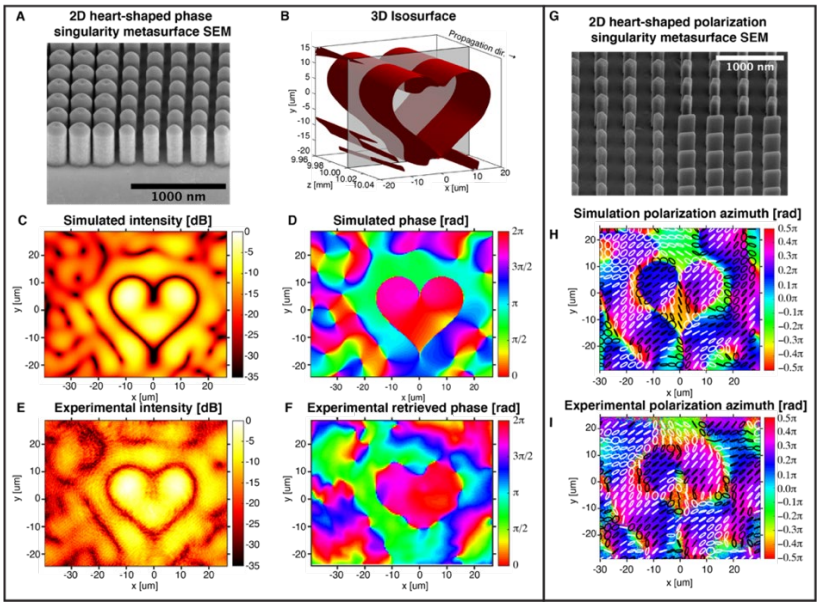

Fig. 14 Experimental realizations of 2D singularity structures. (**A)** Micrograph of a pillar metasurface that produces a 2D heart-shaped phase singularity. (**B)** 3D isosurface of the low-intensity points of the 2D phase singularity. (**C-D)** Simulated and (**E-F**) experimental intensity and phase profiles at axial plane z=10 mm of the singularity. (**G)** Micrograph of a polarization metasurface that produces a 2D heart-shaped polarization singularity. (**H-I)** Simulated and experimental polarization azimuth profile at axial plane z=10 mm. The ellipses in the foreground are local polarization ellipses (black: $s_3 \geq 0$, white: $s_3 < 0$).

Publications

1, Ahmed H. Dorrah and Federico Capasso "Tunable structured light with flat optics." *Science*, 376, 6591 (2022) Invited review

2. Noah A. Rubin, Paul Chevalier, Michael Juhl, Michele Tamagnone, Russell Chipman, and Federico Capasso. 3/8/2022. "Imaging polarimetry through metasurface polarization gratings." *Optics Express*, 30, 9389 (2022)

3. Noah A. Rubin, Zhujun Shi, and Federico Capasso. 1/3/2022. "Polarization in diffractive optics and metasurfaces." *Advances in Optics and Photonics,* 13, 836 (2022) Invited Review

4. Aun Zaidi, Noah A. Rubin, Ahmed H. Dorrah, Joon-Suh Park, and Federico Capasso "Generalized polarization transformations with metasurfaces." *Optics Express*, 29, 39065 (2021)

6. Ahmed H Dorrah, Noah A Rubin, Michele Tamagnone, Aun Zaidi, and Federico Capasso, "Structuring total angular momentum of light along the propagation direction with polarization-controlled meta-optics." *Nature Communications*, 12, 6249 (2021)

7. Noah A. Rubin, Aun Zaidi, Ahmed H. Dorrah, Zhujun Shi, and Federico Capasso “Jones matrix holography with metasurfaces.” *Science Advances,* 7, eabg7488 (2021)

8. Soon Wei Daniel Lim, Joon-Suh Park, Maryna L. Meretska, Ahmed H. Dorrah, and Federico Capasso “Engineering phase and polarization singularity sheets.” *Nature Communications*, 12, 4190 (2021).

9. Christina Spägele, Michele Tamagnone, Dmitry Kazakov, Marcus Ossiander, Marco Piccardo, and Federico Capasso, “Multifunctional wide-angle optics and lasing based on supercell metasurfaces.” *Nature Communications,* 12, 3787 (2021)

10. Ahmed H. Dorrah, Noah A. Rubin, Aun Zaidi, Michele Tamagnone, and Federico Capasso “Metasurface optics for on-demand polarization transformations along the optical path.” *Nature Photonics* 15, 287 (2021)

11. Zhujun Shi, Alexander Y. Zhu, Zhaoyi Li, Yao-Wei Huang, Wei Ting Chen, Cheng-Wei Qiu, and Federico Capasso. 2020. “Continuous angle-tunable birefringence with freeform metasurfaces for arbitrary polarization conversion.” *Science Advances*, 6, 23 (2020)

12. Hend Sroor, Yao-Wei Huang, Bereneice Sephton, Darryl Naidoo, Adam Valles, Vincent Ginis, Cheng-Wei Qiu, Antonio Ambrosio, Federico Capasso, and Andrew Forbes. “High-purity orbital angular momentum states from a visible metasurface laser.” *Nature Photonics,* 14, 498 (2020)

Patents

1. Noah A. Rubin, Aun Zaidi, and Federico Capasso, "Jones Matrix Holography with Metasurfaces", PCT/US21/65231

This patent discloses holograms whose far-fields implement parallel polarization analysis and custom waveplate-like behavior. Additionally, the systems and methods of the present disclosure relate to generalized polarization transformations with metasurfaces. They can be used in applications such as polarization aberration correction in imaging systems and experiments that can use novel and compact polarization detection and control.

2. Noah A. Rubin, Paul Chevalier, and Federico Capasso, "Systems and Methods of Imaging Polarimetry Through Metasurface Polarization Gratings", US 63/225,162

This patent discloses an attachment for an intensity-only sensor in an imaging device including a polarization-sensitive diffraction grating configured to receive incident light from a scene, and to modify the incident light to simultaneously (e.g., concurrently, within a same time duration, etc.) produce a plurality of non-overlapping images of the scene, each of a different diffraction order, on the intensity-only sensor to facilitate full-Stokes imaging polarimetry, and a first adjustment mechanism configured to control at least one of: vignetting of the plurality of non-overlapping images on the intensity-only sensor, or an object distance of the imaging device.

3. Federico Capasso, Dmitry Kazakov, Marco Piccardo, Christina Maria Spaegele and Michele Tamagnone “Wavelength tunable metasurface external cavity laser” PCT/US21/31423

This patent discloses dispersive reflective and transmissive metasurfaces, wavelength-tunable lasers systems incorporating these metasurfaces and methods to manufacture, arrange, control and align these systems are provided. Detailed system, methods and configurations to tune the wavelength, suppress/induce laser mode hopping control the polarization of the emitted light and couple different lasers are also disclosed. The metasurfaces used in these systems created wavelength-dependent and/or polarization dependent feedback which is back-reflected to the laser/gain medium/chip/device, which determines the lasing wavelength and/or polarization.

Awards

Federico Capasso, 2021 *Ives Medal and Jarus Quinn Prize of OSA* "for seminal and wide-ranging contributions to optical physics, quantum electronics and nanophotonics"

Federico Capasso, 2021 *26th Micro-optics Conference Award "*for pioneering contributions to quantum cascade lasers, plasmonic and metamaterials" Hamamatsu City, Japan

Federico Capasso, 2020, *IEEE Italy Honorary Award* "for outstanding and pioneering contributions to the physics of quantum confined photonic systems and their applications, ranging from band-structure engineering to the invention of Quantum Cascade Lasers, and for the engineering of metasurfaces"